

Adaptive quantum optics with spatially entangled photon pairs

Hugo Defienne,^{1*} Matthew Reichert,¹ Jason. W. Fleischer¹

¹Department of Electrical engineering, Princeton University, Princeton, 08540

*To whom correspondence should be addressed; E-mail: defienne@princeton.edu.

Light shaping facilitates the preparation and detection of optical states and underlies many applications in communication, computing and imaging. In this work, we generalize light shaping to the quantum domain. We show that patterns of phase modulation for classical laser light can also shape higher orders of spatial coherence, allowing deterministic tailoring of high-dimensional entanglement. By modulating spatially entangled photon pairs, we create periodic, topological, and random patterns of quantum illumination, without effect on intensity. We then structure the quantum illumination to simultaneously compensate for entanglement that has been randomized by a scattering medium and to characterize the medium's properties via a quantum measurement of the optical memory effect. The results demonstrate fundamental aspects of spatial coherence and open the field of adaptive quantum optics.

Key words

adaptive optics ; quantum optics ; coherent control ; entanglement ; wavefront shaping ; scattering media ; memory effect ; photon pairs

Manuscript

Light shaping is indispensable in many areas of optics. Examples range from the pioneering works of Gabor holography (1) and Zernike phase masks (2) to the recent breakthroughs enabled by spatial light modulators (SLMs) (3). Static SLM patterns have led to advanced pulse shaping (4), super-resolution microscopy (5), and 3D surface imaging, while dynamic patterns underlie video projection and adaptive optics. All of these methods can be used for, and be enhanced by, quantum illumination. Indeed, wavefront shaping has been used to manipulate orbital angular momentum modes (OAMs) of quantum light (6, 7) and to pre-compensate photon scattering in disordered media (8, 9), but to date structure has been imposed independently on each photon of an entangled pair. This restriction was due partly to the use of the other photon for heralding and partly due to the extraordinary difficulty of measuring higher-order spatial coherence. The manipulation has therefore been classical, as there is no substantial difference between shaping the wavefront of a single photon and that of coherent light; rather, true quantum control arises from shaping the correlations within the joint probability distribution. Here, we consider spatially entangled photon pairs and experimentally structure second-order spatial coherence across the entire biphoton distribution function.

Intuition for quantum wavefront shaping follows from the generalized concept of optical coherence (10). First-order coherence of laser light allows intensity shaping by phase modulation of the angular spectrum. For second-order coherence, phase modulation acts on the two-photon wavefunction of spatially entangled photon pairs, which has repercussions on intensity correlations (i.e. coincidences) in the reciprocal space. This means that a given pattern on an SLM can be used to shape both classical and quantum light, as long as measurements are performed in their respective region of coherence. This correspondence is remarkable, as classical methods are exponentially easier to perform: their signal is higher and their measurements simpler. Classical control and feedback are thus exponentially quicker. In practice, optimization in the quantum domain can be bypassed, as quantum signals can piggyback on

the classical parameters. The result is classical design for quantum resources, enabling the highest orders of performance with the lowest order of wavefront manipulation.

In the experiments, we use a phase-only SLM to control the phase of spatially entangled photon pairs and measure its amplitude in the far field (Figure 1). In the case of perfectly correlated photons (11), programming a phase pattern $\phi(\mathbf{r})$ tailors the two-photon field Ψ in the reciprocal space as

$$\Psi(\boldsymbol{\theta}_1, \boldsymbol{\theta}_2) \propto \iint e^{2i\phi(\mathbf{r})} e^{-\frac{2\pi}{\lambda}i\mathbf{r}[\boldsymbol{\theta}_1+\boldsymbol{\theta}_2]} d\mathbf{r} \quad (1)$$

where $\boldsymbol{\theta} = \mathbf{k}\lambda/2\pi$ is the angular spectrum (AS) of photons, \mathbf{k} the momentum and λ the wavelength (12). As shown in Figure 1.a, the experimental setup is built analogously to a conventional beam shaping system, but the laser is substituted by a quantum source. Spatially entangled photon pairs are generated by type-I spontaneous parametric down conversion (SPDC) in a β -barium borate (BBO) crystal pumped by a collimated continuous-wave laser at 403 nm. Near-degenerate down-converted photons are selected via spectral filters (SF) at $\lambda = 806 \pm 1.5$ nm. The output face of the crystal is first imaged onto a phase-only SLM that is itself imaged onto another optical plane (dashed square), where a thin scattering medium will be inserted in the second part of this work. One last lens performs a Fourier transform to map the AS of photons onto the pixels of an electron-multiplied charge-coupled-device (EMCCD) camera. The camera allows (a) direct intensity measurements, providing conventional intensity images $I(\boldsymbol{\theta})$, and (b) correlation intensity measurements, giving the joint probability distribution of photon pairs $\Gamma(\boldsymbol{\theta}_1, \boldsymbol{\theta}_2) = |\Psi(\boldsymbol{\theta}_1, \boldsymbol{\theta}_2)|^2$ (13).

Experimental results are shown in Figure 2. When no phase modulation is applied on the SLM, it acts as a mirror, and correlations between photon pairs result only from momentum conservation imposed by the pair generation process (Figure 2.a1): when the first photon of a pair is emitted at angle $\boldsymbol{\theta}$, its twin is generated at the opposite angle $-\boldsymbol{\theta}$. This anti-correlation property is visible on the conditional projection $\Gamma(\boldsymbol{\theta}_1|\boldsymbol{\theta}_A)$ (Figure 2.a3) where the maximum of probability is located exactly at $\boldsymbol{\theta}_1 = -\boldsymbol{\theta}_A$ ($\boldsymbol{\theta}_A = (1.6 \text{ mrd}, 1.1 \text{ mrd})$ is chosen arbitrarily). When a sinusoidal phase $\phi(x, y) = \pi/2 [\cos(2\pi y/\Lambda) + 1]$ ($\Lambda = 1.2\text{mm}$) is programmed onto the SLM (Figure 2.b1), the direct intensity image does not change

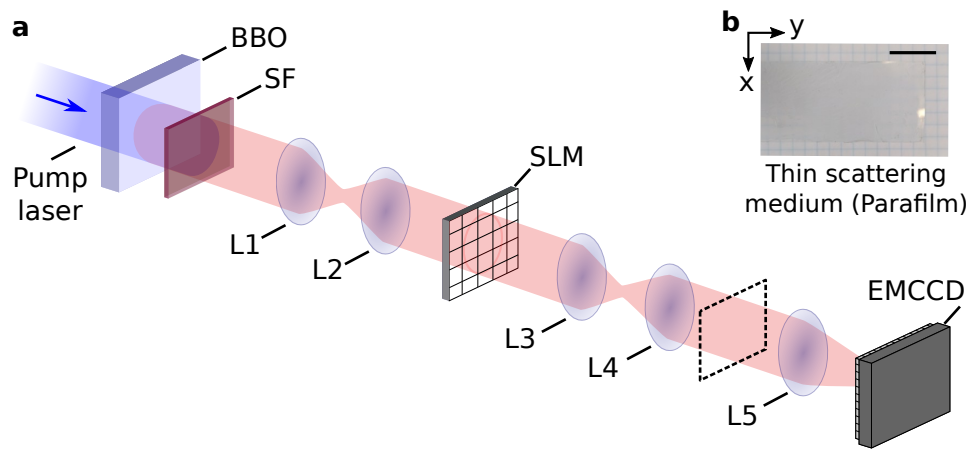


Figure 1: **Schematic of the experiment.** (a) Spatially entangled photon pairs are generated by type-I SPDC in a β -barium borate (BBO) crystal pumped by a collimated continuous-wave laser at 403 nm. Collinear near-degenerate down-converted photons are selected via spectral filters (SF) at 806 ± 3 nm. Lenses L_1 and L_2 image the output surface of the crystal onto the SLM. L_3 and L_4 image the modulated photons into another optical plane (dashed line), where a scattering medium can be inserted. L_5 forms an image of the angular spectrum of photon pairs onto an EMCCD camera. The camera enables both direct and correlation intensity measurements. The thin scattering medium (b) consists of a layer of Parafilm placed on a glass microscope slide. Scale bar is 2cm. For clarity, the SLM is represented in transmission, while it operates in reflection.

(Figure 2.b2), while the correlation structure between photons does. $\Gamma(\theta_1|\theta_A)$ takes a comb-like structure centered around $-\theta_A$ with a period proportional to λ/Λ (Figure 2.b3). Since $\theta_1 + \theta_2$ and r are conjugate variables in the Fourier transform (Equation 1), the sum coordinate offers another appropriate basis to observe correlation modulation, as shown in Figure 2.a4 and b4. In a last example, a helical phase pattern $\phi(x, y) = 3 \arctan(y/x)$ programmed on the SLM (Figure 2.c1) generates a ring on the sum-coordinate projection (Figure 2.c4). Interestingly, the same experiment performed using classical coherent light (Figure 2.c3) produces a ring with half the diameter. This factor of two highlights a fundamental difference between classical coherence and quantum coherence of photon pairs, in that the latter accumulate twice the phase during propagation (14).

Figure 2.c also highlights the fact that knowledge of the classical wavefront can be used to engineer the appropriate quantum structure. This is of enormous benefit for adaptive optics, as the measurement-feedback loop in the quantum case would be practically impossible without it (the Hilbert space is too large, the signal-to-noise ratio too small, etc). Nevertheless, this field is of growing importance, e.g. for sending images and secure information through turbulence (15, 16). In Figure 3, we show a paradigm example of this problem: re-focusing spatial entanglement that has been randomized by a scattering medium. In this experiment, a layer of parafilm is inserted in an image plane (dashed square) of the setup (Figure 1). A comparison between conditional images $\Gamma(\theta_1|\mathbf{0})$ taken without the medium (Figure 3.a) and after its insertion (Figure 3.b) shows a loss of the near-perfect anti-correlations in the AS of photons in favor of a randomly distributed probability pattern called two-photon speckle (17). To overcome this speckle, we leverage the classical-quantum correspondence in Figure 2 and the well-established techniques of classical wavefront shaping (18) to first determine an optimized phase pattern using a coherent source that has the same properties than the photon pairs. This can be done very quickly by iterative optimization on the laser intensity at a given pixel of the camera (12, 19). *The same pattern on the SLM is then used to shape the quantum illumination* (Figure 3.c). As shown in Figure 3.d, the conditional image $\Gamma(\theta_1|\theta_2 = \mathbf{0})$ measured at the output shows an intense peak of probability, demonstrating the

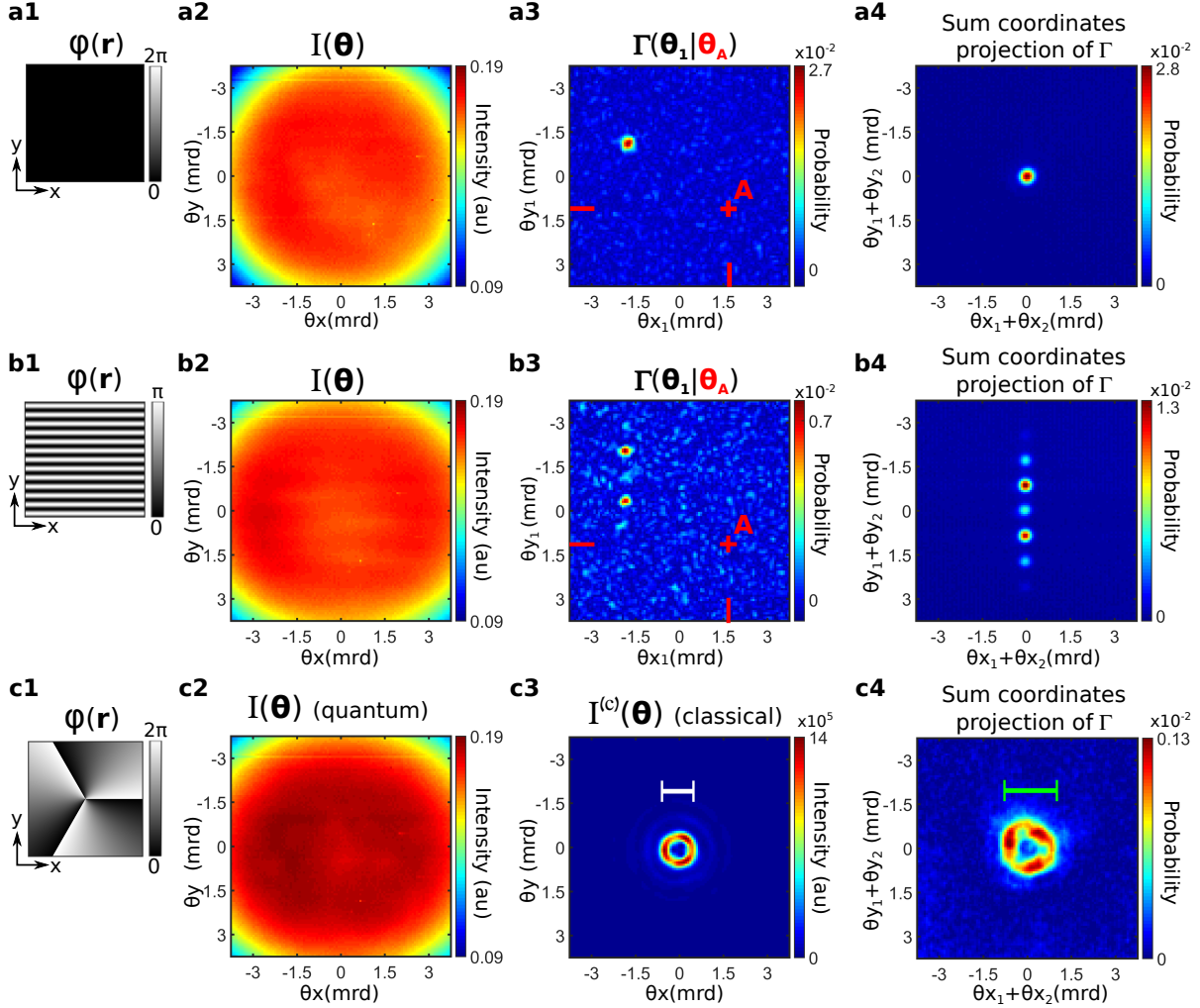


Figure 2: **Structuring entanglement by wavefront shaping.** Direct intensity images I and joint probability distributions Γ are measured under photon-pair illumination using an EMCCD camera (13). Without shaping (a1), angular-spectrum anti-correlations are visible on a conditional image $\Gamma(\theta_1|\theta_A)$ taken for an arbitrarily chosen position $\theta_A = (1.6 \text{ mrd}, 1.1 \text{ mrd})$ (a3) and on the sum-coordinate projection of Γ (a4). A sine phase mask (b1) programmed on the SLM tailors the spatial structure of entanglement into a comb-like pattern, visible on both the conditional image (b3) and on the sum-coordinate projection (b4). A helical SLM phase pattern (c1) produces a ring structure in the sum coordinate projection (c4) with a ring diameter 1.93mrad (green scale bar). The same experiment performed under classical illumination creates a ring in the direct image (c3) with half the diameter 1.04mrad (white scale bar). All direct images recorded under quantum illumination (a2,b2,c2) are independent of the programmed phase patterns.

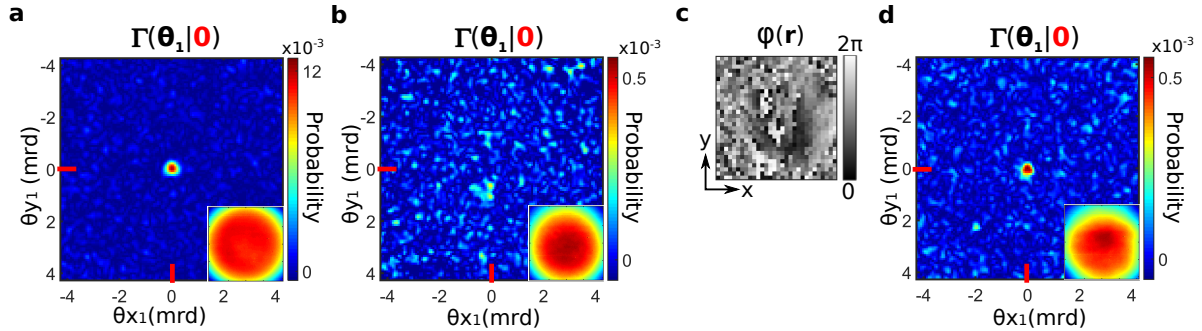


Figure 3: **Focusing entanglement through a thin scattering medium.** Conditional image $\Gamma(\theta_1|\mathbf{0})$ measured without the medium (a) shows an intense probability peak at $\theta_1 = \mathbf{0}$. After insertion of the medium, the peak disappears and is replaced by a two-photon speckle pattern (b). Programming the optimized phase pattern (c), previously determined using classical coherent light, allows re-focusing of the entanglement at the output of the medium (d). The shape of the direct intensity image measured at the output (insets) is not affected by the presence of the medium or by the shaping process.

re-focusing of pairs in coincidence. As before, quantum coherence is evident in the two-photon field only; the pattern of the direct intensity image measured at the output is affected by neither the medium nor the wavefront shaping process (insets).

Optical properties of the scattering medium itself can be characterized by a two-point correlation function as well. This can be measured with classical illumination by tilting the pre-compensated wavefront at the input and watching the fall-off in peak intensity at the output (12). The persistence the re-focusing process with the increase of illumination angle is known as the optical memory effect of the medium, and depends on its complexity (20). Knowledge of the memory effect is inherent in the case of quantum illumination. At the first-order, spatially entangled photons are incoherent [$g^{(1)}(\mathbf{r}_1, \mathbf{r}_2) = \delta(\mathbf{r}_1 - \mathbf{r}_2)$ for perfectly-correlated pairs] and illuminate the medium with a large angular spectrum (21); Consequently, when structuring quantum light, re-focusing of photon pairs in coincidence occurs not only at the targeted position ($\theta_2 = \mathbf{0}$) but for larger angles as well, and the memory effect is thus completely characterized by a single measurement of the joint probability distribution. In Figure 4, we show the optical memory effect visualized along the y -axis (chosen arbitrarily) by projecting the joint probability distribution onto two columns of pixels selected symmetrically from the direct intensity im-

age ($\theta_{x_1} = -0.07$ mrd and $\theta_{x_2} = 0.07$ mrd). As shown in Figure 4.c, we observe the presence of a short anti-diagonal at the center of the image, confirming that anti-correlations between pairs are maintained by the wavefront compensation over a finite angular range $\Delta\theta_y$ (in contrast with anti-correlations over the full angular spectrum observed without the medium in Figure 4.b). A quantitative analysis performed by fitting the focusing ratio $\Gamma(\theta_{x_1} = 0, \theta_y | \theta_{x_2} = 0, -\theta_y) / \Gamma(0|0)$ with a theoretical model derived for the quantum case (12) provides an estimation of the memory effect angle $\Delta\theta_y = 1.01 \pm 0.1$ (Figure 4.e - red curve). A comparison with a conventional measurement of the memory effect performed with classical light (blue curve) shows that the nonlocal sampling of the medium by photon pairs (Figure 4.d) gives a faster decorrelation.

Deterministic shaping of entanglement is a promising technique for fundamental physics investigations, such as triggering of coherent processes in molecules (22) and plasmons (23), and manipulating optical states for quantum storage (24) and processing (25). It provides a straightforward solution for high-dimensional, entanglement-based quantum communications through imperfect fibers (26) and turbulence (27). While our experiment involve only spatial entanglement of photon pairs, the methods extend easily to higher orders of quantum coherence (28) and to other degrees of freedom, such as polarization or time (29). With proper design, adaptive quantum optics can optimize systems where quantum light is beneficial and enable systems where controlled entanglement is required.

Acknowledgment

This work was supported by the grants AFOSR FA9550-14-1-0177 and DARPA HR0011-16-C-0027.

Author contributions

H.D conceived and performed the experiment; M.R and H.D developed the theory ; all authors analyzed the data and co-wrote the paper.

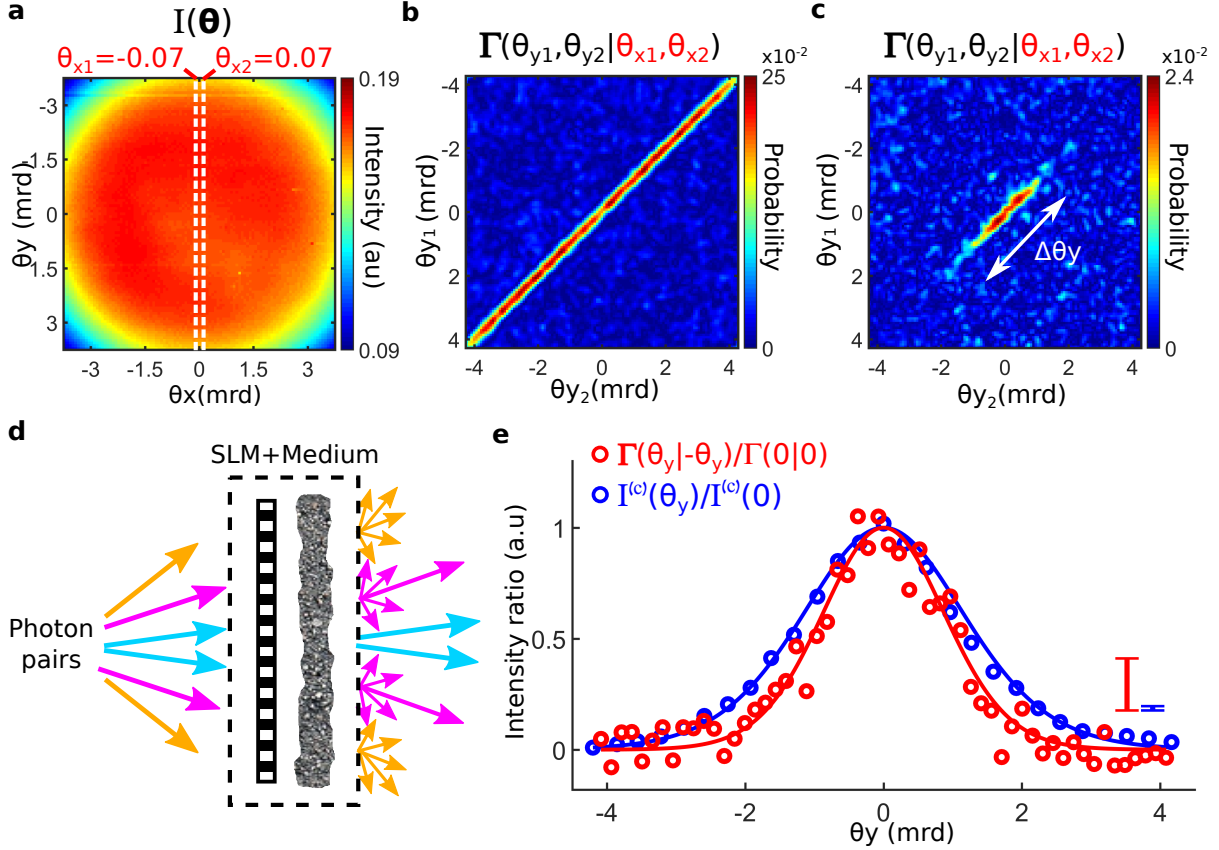


Figure 4: **Characterization of the optical memory effect using quantum illumination.** The joint probability distribution of photon pairs is projected onto two columns of pixels located at $\theta_{x1} = -0.07$ mrd and $\theta_{x2} = 0.07$ mrd on the direct image (a). Without the scattering medium (b), $\Gamma(\theta_{y1}, \theta_{y2} | \theta_{x1} = -0.07, \theta_{x2} = 0.07)$ shows an intense anti-diagonal, that reflects the anti-correlation in the angular spectrum of photon pairs. With the medium (c), the optimization technique reconstructs anti-correlations between pairs only in a limited angular range $\Delta\theta_y$, seen as a reduction of the diagonal length. Programming the optimal phase pattern onto the SLM effectively transforms the thin scattering medium into a transparent medium but with a limited field of view (d). Fitting the focusing ratio $\Gamma(\theta_{x1} = 0, \theta_y | \theta_{x2} = 0, -\theta_y) / \Gamma(0|0)$ (red circles) with its corresponding theoretical model (red line) gives $\Delta\theta_y = 1.01 \pm 0.1$ mrd (e). Classical measurement of the memory effect is represented on the same graph (blue circle) together with its corresponding theoretical model (blue line). For clarity, error bars are shown above the graphs.

References

1. D. Gabor, *Nature* **161**, 777 (1948).
2. F. Zernike, *Science* **121**, 345 (1955).
3. P. Yeh, C. Gu, *Optics of Liquid Crystal Displays* (Wiley Publishing, 2009), second edn.
4. A. M. Weiner, *Review of Scientific Instruments* **71**, 1929 (2000).
5. T. A. Klar, S. Jakobs, M. Dyba, A. Egner, S. W. Hell, *PNAS* **97**, 8206 (2000).
6. J. Leach, *et al.*, *Science* **329**, 662 (2010).
7. R. Fickler, *et al.*, *Science* **338**, 640 (2012).
8. H. Defienne, M. Barbieri, I. A. Walmsley, B. J. Smith, S. Gigan, *Science Advances* **2**, e1501054 (2016).
9. T. A. W. Wolterink, *et al.*, *Phys. Rev. A* **93**, 053817 (2016).
10. R. J. Glauber, *Physical Review* **130**, 2529 (1963).
11. A. F. Abouraddy, B. E. A. Saleh, A. V. Sergienko, M. C. Teich, *J. Opt. Soc. Am. B, JOSAB* **19**, 1174 (2002).
12. SupplementaryMaterial .
13. M. Reichert, H. Defienne, J. W. Fleischer, *arXiv:1710.01781 [physics, physics:quant-ph]* (2017).
ArXiv: 1710.01781.
14. G. Brida, M. Genovese, I. R. Berchera, *Nature Photonics* **4**, 227 (2010).
15. A. Sit, *et al.*, *Optica, OPTICA* **4**, 1006 (2017).

16. F. Bouchard, *et al.*, *arXiv:1801.10299 [physics, physics:quant-ph]* (2018). ArXiv: 1801.10299.
17. W. H. Peeters, J. J. D. Moerman, M. P. van Exter, *Physical Review Letters* **104** (2010).
18. A. P. Mosk, A. Lagendijk, G. Lerosey, M. Fink, *Nature Photonics* **6**, 283 (2012).
19. I. M. Vellekoop, A. P. Mosk, *Opt. Lett., OL* **32**, 2309 (2007).
20. I. Freund, M. Rosenbluh, S. Feng, *Phys. Rev. Lett.* **61**, 2328 (1988).
21. B. E. A. Saleh, A. F. Abouraddy, A. V. Sergienko, M. C. Teich, *Phys. Rev. A* **62**, 043816 (2000).
22. O. Roslyak, C. A. Marx, S. Mukame, *Phys Rev A* **79**, 33832 (2009).
23. E. Altewischer, M. P. van Exter, J. P. Woerdman, *Nature* **418**, 304 (2002).
24. R. Hildner, D. Brinks, J. B. Nieder, R. J. Cogdell, N. F. v. Hulst, *Science* **340**, 1448 (2013).
25. A. F. Abouraddy, B. E. A. Saleh, G. Giuseppe, K. H. Kagalwala, *Nature Communications* **8**, 739 (2017).
26. L. V. Amitonova, T. B. H. Tentrup, I. M. Vellekoop, P. W. H. Pinkse, *arXiv:1801.07180 [physics, physics:quant-ph]* (2018). ArXiv: 1801.07180.
27. M. Krenn, J. Handsteiner, M. Fink, R. Fickler, A. Zeilinger, *PNAS* **112**, 14197 (2015).
28. T. Nagata, R. Okamoto, J. L. O'Brien, K. Sasaki, S. Takeuchi, *Science* **316**, 726 (2007).
29. A. Pe'er, B. Dayan, A. A. Friesem, Y. Silberberg, *Physical review letters* **94**, 073601 (2005).
30. M. Reichert, H. Defienne, J. W. Fleischer, *arXiv:1802.00489 [physics, physics:quant-ph]* (2018). ArXiv: 1802.00489.
31. M. V. Fedorov, Y. M. Mikhailova, P. A. Volkov, *J. Phys. B: At. Mol. Opt. Phys.* **42**, 175503 (2009).

32. P.-A. Moreau, J. Mougin-Sisini, F. Devaux, E. Lantz, *Phys. Rev. A* **86**, 010101 (2012).
33. D. S. Tasca, *et al.*, *Nature Communications* **3**, 984 (2012).
34. J. C. Howell, R. S. Bennink, S. J. Bentley, R. W. Boyd, *Phys. Rev. Lett.* **92**, 210403 (2004).
35. E. Small, O. Katz, Y. Silberberg, *Nature Photonics* **6**, 549 (2012).
36. S. Feng, C. Kane, P. A. Lee, A. D. Stone, *Phys. Rev. Lett.* **61**, 834 (1988).

Supplementary Materials: Adaptive quantum optics with spatially entangled photon pairs

Supplementary text

Figs. S1 to S9

Movies. M1 to M5

References (30 - 36)

1 Additional experimental details

The β -barium borate crystal (BBO) used in our experimental setup (Figure 1) has dimensions of $3 \times 3 \times 1$ mm³. The collimated pump beam is a diode laser centered at 403 nm (Coherent), with a total intensity of 50mW and a diameter of 2.7mm full-width half-maximum (FWHM). The crystal is tilted slightly with an angle of approximately 3° to ensure collinear phase matching of generated photons. Spectral filters (SF) are composed of two high-pass filters with a cutoff at 750nm (Thorlabs) and one bandpass filter 806 ± 3 nm (Semrock). The first two lenses have focal lengths of $L_1 = 75$ mm and $L_2 = 300$ mm, which enables illumination of approximately $16 \cdot 10^4$ pixels of the SLM (Pluto NIR-II from Holoeye), representing an active area of 3.2mm. The three other lenses have focal lengths of $L_3 = 300$ mm, $L_4 = 250$ mm and $L_5 = 175$ mm.

2 Additional details on measuring the joint probability distribution of photon pairs with an EMCCD camera

2.1 Measurement process

We use an EMCCD Andor Ixon Ultra 888 to measure the joint probability distribution Γ of spatially entangled photon pairs using a technique described in (13). A simplified schematic of the measurement process is illustrated in Figure S1.a. The camera was operated at -60°C , with a horizontal pixel shift readout rate of 10Mhz, a vertical pixel shift every $0.6 \mu\text{s}$ and a vertical clock amplitude voltage of +2V

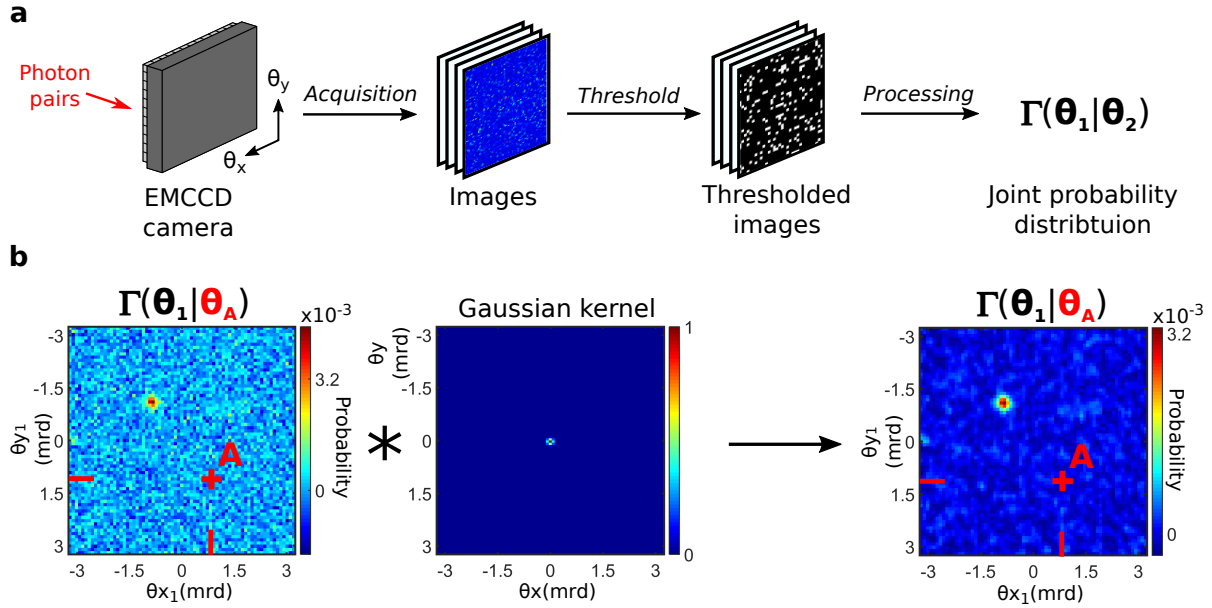


Figure S1: **Measuring the joint probability distribution of photon pairs with an EMCCD camera.** (a) Simplified schematic of the EMCCD camera operation to reconstruct the joint probability distribution (JPD) of photon pairs. After acquiring a large set of images, a threshold process is applied to each image to discriminate electronic noise from signals generated by detection of photon on the camera pixels. The JPD is then calculated using the formula provided in (13). (b) A noise reduction process can be used on the conditional images by using a low-pass frequency filter. This operation corresponds to a convolution of the images with a Gaussian kernel, and enabling an effective increase of the signal-to-noise ratio (SNR) at the expense of a small loss in resolution.

above the factory setting. When the camera is illuminated by photon pairs, a large set of images is first collected using an exposure time chosen to optimize the quality of the measured joint probability distribution (30). A threshold is then applied on all the images to discriminate output values that originate from the detection of a photon, from those due to electronic noise. Processing the set of thresholded images using the formula provided in (13) finally enables to reconstruct Γ .

2.2 Projections of the joint probability distribution

In our experiment, Γ takes the form of a 4-dimensional matrix containing $(125 \times 125)^4 \sim 10^{10}$ elements, where 125×125 corresponds the size of the illuminated region of the camera sensor. The information content of Γ is analyzed using four types of projections:

1. The sum-coordinate projection, defined as

$$\Gamma_S(\boldsymbol{\theta}_+) = \sum_{\boldsymbol{\theta}} \Gamma(\boldsymbol{\theta}_+ - \boldsymbol{\theta}, \boldsymbol{\theta}) \quad (\text{S1})$$

It represents the probability of detecting pairs of photons generated in all symmetric directions relative to the mean angle $\boldsymbol{\theta}_+$.

2. The minus-coordinate projection, defined as

$$\Gamma_M(\boldsymbol{\theta}_-) = \sum_{\boldsymbol{\theta}} \Gamma(\boldsymbol{\theta}_- + \boldsymbol{\theta}, \boldsymbol{\theta}) \quad (\text{S2})$$

It represents the probability for two photons of a pair to be detected in coincidence between pairs of pixels separated by an oriented distance $\boldsymbol{\theta}_-$.

3. A conditional image $\Gamma(\boldsymbol{\theta}_1|\boldsymbol{\theta}_2)$ is a slice of Γ normalized to its marginal probability:

$$\Gamma(\boldsymbol{\theta}_1|\boldsymbol{\theta}_2) = \frac{\Gamma(\boldsymbol{\theta}_1, \boldsymbol{\theta}_2)}{\sum_{\boldsymbol{\theta}_1} \Gamma(\boldsymbol{\theta}_1|\boldsymbol{\theta}_2)} \quad (\text{S3})$$

It represents the probability of detecting one photon at position $\boldsymbol{\theta}_1$ given that the other arrives at position $\boldsymbol{\theta}_2$.

4. A projection of Γ onto two columns of pixels located at θ_{x_1} and θ_{x_2} is defined as:

$$\Gamma(\theta_{y_1}, \theta_{y_2}|\theta_{x_1}, \theta_{x_2}) = \frac{\Gamma(\theta_{x_1}, \theta_{y_1}, \theta_{x_2}, \theta_{y_2})}{\sum_{\theta_{y_1}, \theta_{y_2}} \Gamma(\theta_{x_1}, \theta_{y_1}, \theta_{x_2}, \theta_{y_2})} \quad (\text{S4})$$

Similarly, a projection of Γ onto two lines of pixels located at θ_{y_1} and θ_{y_2} is defined as:

$$\Gamma(\theta_{x_1}, \theta_{x_2}|\theta_{y_1}, \theta_{y_2}) = \frac{\Gamma(\theta_{x_1}, \theta_{y_1}, \theta_{x_2}, \theta_{y_2})}{\sum_{\theta_{x_1}, \theta_{x_2}} \Gamma(\theta_{x_1}, \theta_{y_1}, \theta_{x_2}, \theta_{y_2})} \quad (\text{S5})$$

These projections are bi-dimensional joint probability distributions between two horizontal (or vertical) spatial axes.

2.3 Post-processing

The signal-to-noise (SNR) ratio in Γ increases with the number of acquired images (on the order of 10^7 in our experiment). As shown in Figure S1.b, a low-pass frequency filter process can be applied to the conditional images to reduce the noise and increase the SNR, at the expense of a small loss in resolution.

3 Additional details relative to spatial entanglement between photon pairs

The wavefunction of photon pairs generated by SPDC can be modeled by a double gaussian (31). At the output surface of the crystal, it takes the form:

$$\Psi_0(\mathbf{r}_1, \mathbf{r}_2) \propto \int e^{-\frac{|\mathbf{r}_1 - \mathbf{r}_2|^2}{2\sigma_{r_-}^2}} e^{-\frac{\pi|\mathbf{r}_1 + \mathbf{r}_2|^2\sigma_{\theta_+}^2}{\lambda}} d\mathbf{r}_1 d\mathbf{r}_2 \quad (\text{S6})$$

where σ_{r_-} and σ_{θ_+} are the position and the angular correlation widths.

3.1 Angular correlation

As shown in Figure 2, photon pairs are anti-correlated in their angular spectrum because of momentum conservation in the pair-generation process. The angular correlation width is directly estimated from the width of the peak located at the center of the sum-coordinate projection of Γ (Figure 2.a4) : $\sigma_{\theta_+} = 0.118 \pm 0.001$ mrd (32, 33).

3.2 Position correlation

As illustrated in Figure S2.a, correlation of position between photon pairs is characterized by introducing a lens L_6 before the camera to create another two-lens system (L_5 and L_6). This configuration forms an image of the output surface of the crystal on the EMCCD camera (Figure S2.b). Conditional image $\Gamma(\mathbf{r}_1|\mathbf{r}_B)$ with $\mathbf{r}_B = (-250, 390)$ μm (Figure S2.c) reveals strong correlations between positions of photon pair: when the first photon is detected at position \mathbf{r}_B , the second is detected with a high probability at the same position. The bright peak at the center of the projection of Γ on the minus-coordinate basis (Figure S2.d) provides a measurement of the position correlation width $\sigma_{r_-} = 39 \pm 2$ μm (32, 33).

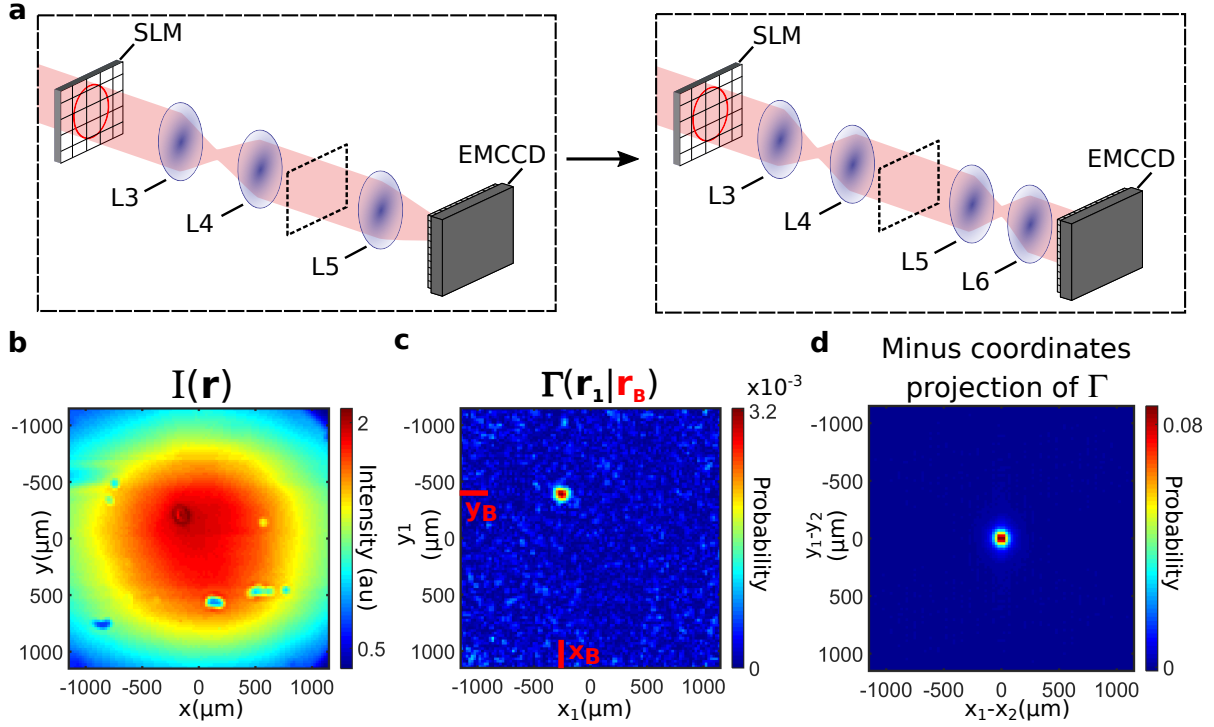


Figure S2: **Position correlations between photon pairs.** (a) Insertion of a lens $L_6 = 175\text{mm}$ in the experimental setup forms an image of the output surface of the crystal on the EMCCD camera. A direct image measured at the output shows the surface of the crystal (b), where dark spots correspond to dust. Conditional image $\Gamma(\mathbf{r}_1|\mathbf{r}_B)$ with $\mathbf{r}_B = (-250, 390) \mu\text{m}$ (c) together with the minus-coordinate projection of Γ (d) reveal correlations between positions of photon pairs and provides a measure of the position correlation width $\sigma_{r_-} = 39 \pm 2 \mu\text{m}$.

3.3 Degree of entanglement

Values of σ_{r_-} and σ_{θ_+} can be used to estimate the Schmidt number K that characterizes the degree of entanglement in the state (31)

$$K = \left(\frac{\sigma_{r_+}^2 + \sigma_{r_-}^2}{2\sigma_{r_-}\sigma_{r_+}} \right)^2 = 194 \pm 26 \quad (\text{S7})$$

where $\sigma_{r_+} = \lambda/(2\pi\sigma_{\theta_+})$. It is important to note that, because the SLM only performs linear unitary operations, shaping the structure of entanglement does not change the total amount of entanglement K carried by the pairs.

3.4 EPR non-locality

Values of correlation widths can also be used to calculate the uncertainty

$$\frac{2\pi}{\lambda}\sigma_{\theta_+}\sigma_{r_-} = 3.6 \cdot 10^{-2} \pm 2.10^{-3} \ll \frac{1}{2} \quad (\text{S8})$$

which demonstrates that the transverse degrees of freedom of photon pairs exhibit EPR non-locality (34).

4 Tailoring spatial entanglement of photon pairs by wavefront shaping

The first part of this section provides a theoretical derivation of Equation 1. In the second part, we introduce a complementary experimental setup that can be used for shaping of entanglement.

4.1 Theory

Under the paraxial approximation, properties of monochromatic photon pairs with the same polarization and frequency are completely described by a spatial two-photon wavefunction $\Psi(\mathbf{r}_1, \mathbf{r}_2)$, where $\mathbf{r}_1 = (x_1, y_1)$ and $\mathbf{r}_2 = (x_2, y_2)$ are the transverse spatial coordinates in the optical plane. As detailed in (11), evolution Ψ after propagation through a linear optical system with input response function $h(\mathbf{r}', \mathbf{r})$, where $\mathbf{r}(\mathbf{r}')$ are transverse spatial coordinates in the input (output) optical plane, is calculated as:

$$\Psi'(\mathbf{r}_1', \mathbf{r}_2') = \iint h(\mathbf{r}_1', \mathbf{r}_1)h(\mathbf{r}_2', \mathbf{r}_2)\Psi(\mathbf{r}_1, \mathbf{r}_2)d\mathbf{r}_1d\mathbf{r}_2 \quad (\text{S9})$$

where Ψ (Ψ') is the two-photon wavefunction in the input (output) optical plane. Without losing the generality of the approach, we consider that all the two-lens system (L_1 - L_2 and L_3 - L_4) of our experimental setup are perfect imaging systems with unit magnification: $h(\mathbf{r}', \mathbf{r}) = \delta(\mathbf{r}' - \mathbf{r})$. After being reflected by the SLM, the two-photon wavefunction takes the form

$$\Psi^{(slm)}(\mathbf{r}_1, \mathbf{r}_2) = e^{i\phi(\mathbf{r}_1)} e^{i\phi(\mathbf{r}_2)} \Psi_0(\mathbf{r}_1, \mathbf{r}_2) \quad (\text{S10})$$

where $\phi(\mathbf{r})$ is the phase shift introduced by the SLM at position \mathbf{r} and Ψ_0 is the two-photon wavefunction at the output surface of the crystal. Lens L_5 forms an image of the angular spectrum (AS) of the pairs onto the SLM, which corresponds to performing a Fourier transform

$$h(\mathbf{r}', \mathbf{r}) \propto e^{-i\frac{2\pi}{\lambda f} \mathbf{r}' \cdot \mathbf{r}} \quad (\text{S11})$$

where f is the focal length of L_5 . By introducing the variable $\boldsymbol{\theta} = \mathbf{r}'/f$, the image of Ψ on the camera can be written as

$$\Psi(\boldsymbol{\theta}_1, \boldsymbol{\theta}_2) \propto \iint e^{-i\frac{2\pi}{\lambda} \boldsymbol{\theta}_1 \cdot \mathbf{r}_1} e^{-i\frac{2\pi}{\lambda} \boldsymbol{\theta}_2 \cdot \mathbf{r}_2} e^{i\phi(\mathbf{r}_1)} e^{i\phi(\mathbf{r}_2)} \Psi_0(\mathbf{r}_1, \mathbf{r}_2) d\mathbf{r}_1 d\mathbf{r}_2 \quad (\text{S12})$$

As shown in the previous section, photon pairs generated in our experiment exhibit strong correlations between their transverse position at the output surface of the crystal. Considering the limit of perfect correlations, Ψ_0 can be approximated as

$$\Psi_0(\mathbf{r}_1, \mathbf{r}_2) \approx \delta(\mathbf{r}_1 - \mathbf{r}_2) \quad (\text{S13})$$

allowing the two-photon wave function to take the form written in Equation 1.

4.2 An alternative experimental setup for shaping of entanglement

In the experimental setup shown in Figure 1, the phase of the two-photon wavefunction is modulated in the space of positions to shape its amplitude in momentum space. Similarly, it is possible to modulate the phase of the wave function in momentum space to shape its amplitude in position space. Using

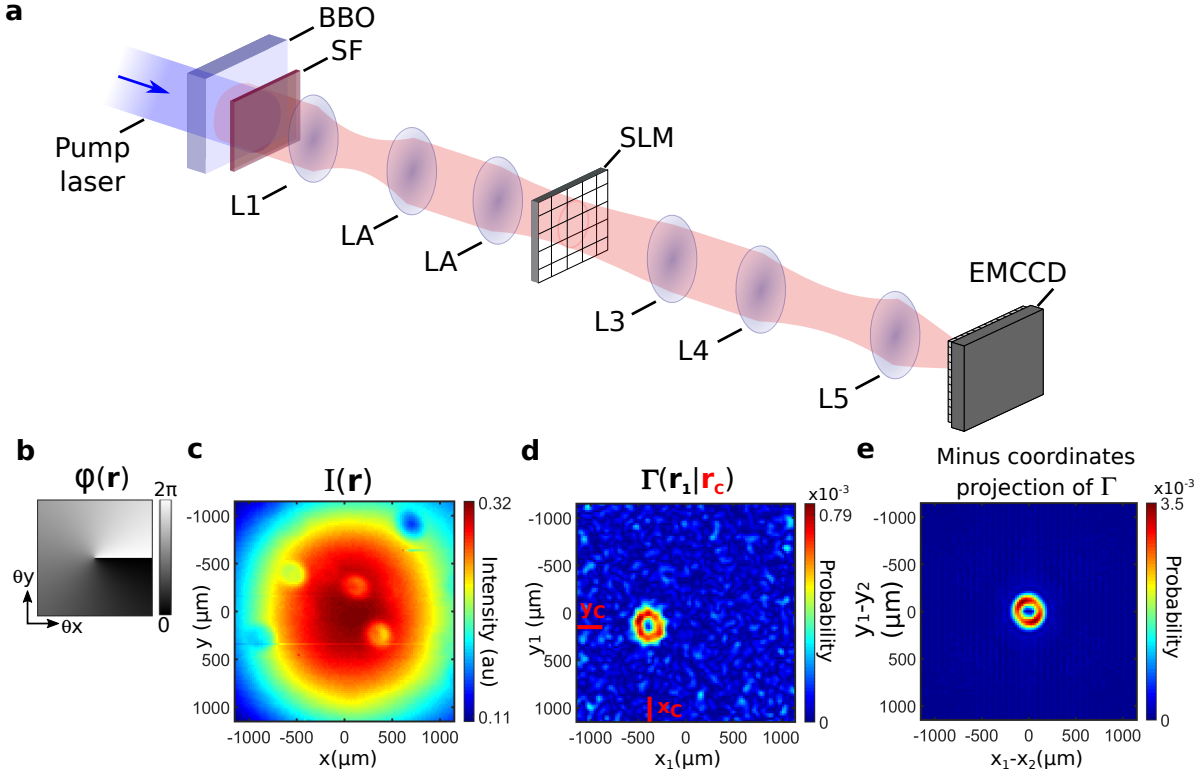


Figure S3: **Shaping the amplitude of the two-photon wavefunction in position space by phase modulation in the momentum domain.** (a) Experimental setup. The angular spectrum of photon pairs is mapped onto the SLM by a set of three lenses (L_1 and $L_A = 150$ mm). Another Fourier transform is then performed by a second set of lenses (L_3, L_4 and L_5). When a helical phase pattern is programmed onto the SLM (b), a ring appears on the conditional image $\Gamma(\mathbf{r}_1|\mathbf{r}_C)$ [taken at an arbitrary position $\mathbf{r}_C = (-386, 136) \mu\text{m}$] (c) and on the projection of Γ in the minus-coordinate basis (d).

the theoretical formalism provided in paragraph 4.1, programming a phase pattern $\phi(\boldsymbol{\theta})$ in momentum tailors the two-photon field in the position domain as

$$\Psi(\mathbf{r}_1, \mathbf{r}_2) \propto \iint e^{i[\phi(\boldsymbol{\theta}) - \phi(-\boldsymbol{\theta})]} e^{-\frac{2\pi}{\lambda} i\boldsymbol{\theta}[\mathbf{r}_1 - \mathbf{r}_2]} d\boldsymbol{\theta} \quad (\text{S14})$$

The corresponding experimental setup is shown in Figure S3.a. When the SLM is programmed with an helical phase pattern $\phi(\theta_x, \theta_y) = \arctan(\theta_y/\theta_x)$ (Figure S3.b), a ring pattern is observed on the conditional image $\Gamma(\mathbf{r}_1|\mathbf{r}_C)$ [taken for $\mathbf{r}_C = (-386, 136) \mu\text{m}$] (Figure S3.c) and on the projection of Γ in the minus-coordinate basis (Figure S3.d).

5 Characterization of the optical memory effect of a thin scattering medium using classical coherent light

This section describes the conventional technique used to characterize the optical memory effect of a thin scattering medium with classical coherent light.

5.1 Illumination with classical coherent source

As shown in Figure S4.a, the source that is used for classical light experiments is a super-luminescent diode (SLED) centered at $811\text{nm} \pm 11\text{nm}$, collimated at the input with a FWHM of 7.5mm. The use of the same band-pass filters (SF ; $\lambda = 806 \pm 1.5 \text{ nm}$) as with the quantum source ensures a near-perfect matching of spectral properties between photon pairs and classical light.

5.2 Focusing light through a scattering medium

Without the scattering medium, classical light is simply concentrated at the center of the direct intensity image recorded by the camera (Figure S4.b). When the medium is inserted and no shaping is applied, a speckle pattern is generated at the output (Figure S4.c). As shown in Figure S4.d, an iterative optimization algorithm (19) enables determination of the optimal phase pattern for re-focusing light through the scattering medium. The absolute enhancement ratio η , defined as the ratio between intensity value at the targeted position after focusing through the medium and the intensity value measured at the same

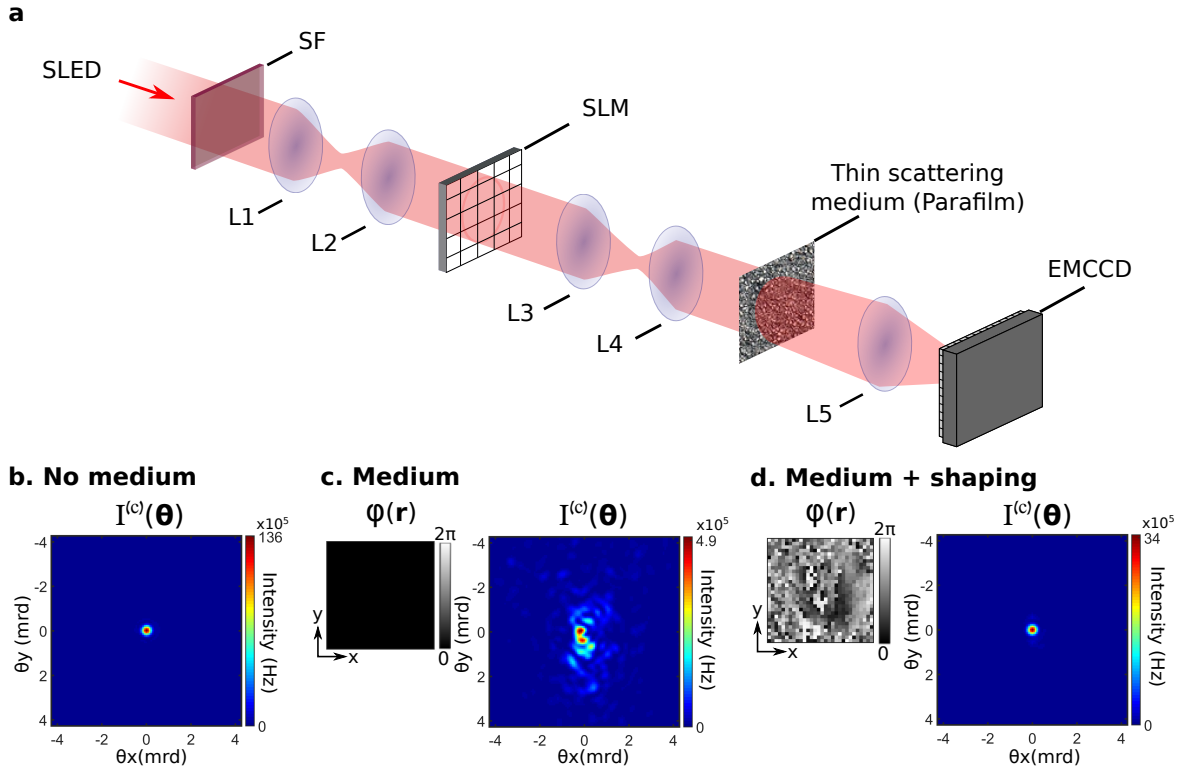


Figure S4: **Focusing classical light through the scattering medium.** (a) To perform experiments with classical light, the photon-pair source is replaced by a collimated super-luminescent diode (SLED) followed by the same spectral filters (SF ; $\lambda = 806 \pm 1.5$ nm). Without the medium, light is simply focused at the center of the camera (b). When the medium is inserted and no shaping is applied, a speckle pattern is generated at the output (c). After performing the optimization process, an phase mask programmed on the SLM re-focuses light at the center of the screen (d).

position without the medium, equals $\eta \approx 0.25$. We observe in Figure 3 that the analogous enhancement ratio measured in the quantum case equals $\eta_q \approx 0.04$, which is on the order of η^2 (as expected when measurement are performed in the coincidence domain).

5.3 Characterization of the optical memory effect

The memory effect of the scattering medium is characterized using the approach described in (35). After the optimization process, intensity at focus is measured while the angle θ of the incident beam is scanned. As shown in Figure S5, this task can be achieved experimentally by programming a linear phase ramp $\phi(x, y) = K_x x + K_y y$ on the SLM, where K_x and K_y set the slope of the ramp. Without the medium

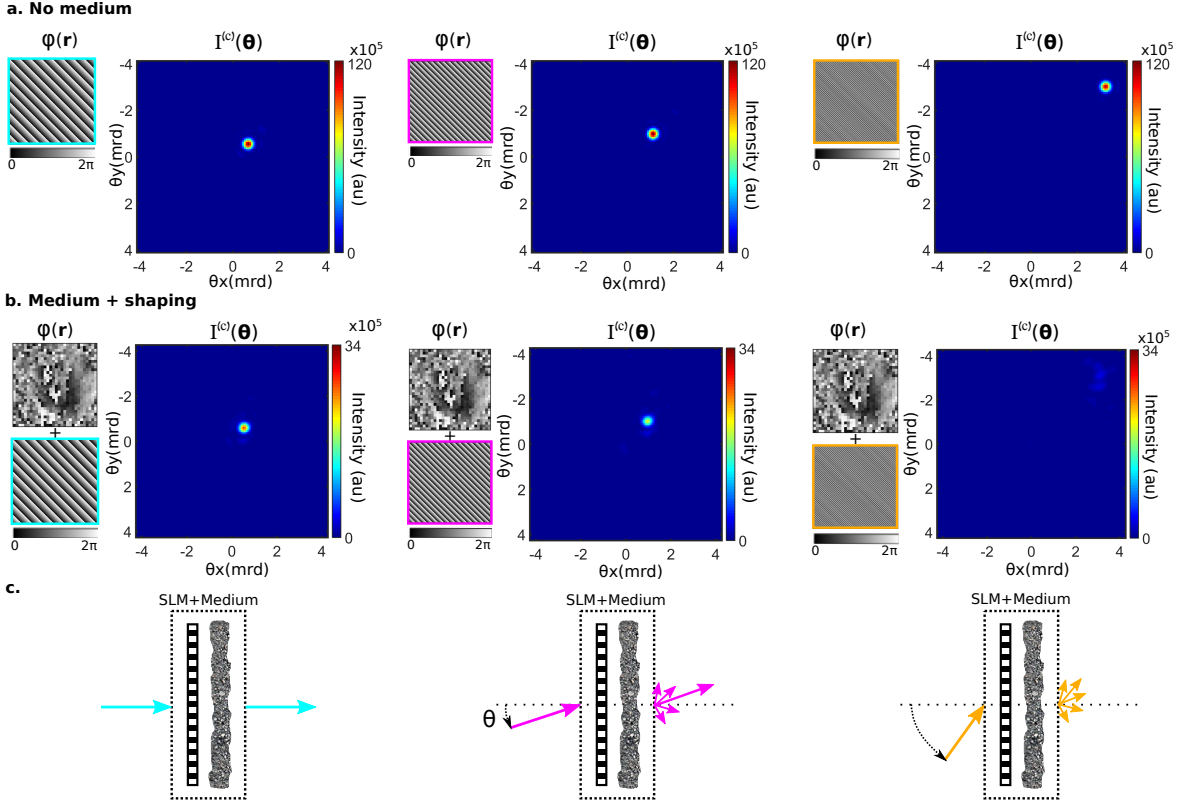


Figure S5: **The optical memory effect.** Without the medium, a linear phase ramp on the SLM produces a shift of the focus spot on the camera (a). When the medium is inserted and the optimization is performed, a shift of the focus spot is achieved by superimposing a phase ramp pattern on the optimized phase mask (b). The decrease of the intensity at focus with increasing angle of illumination is due to the optical memory effect of the medium. The optimized phase pattern effectively transforms the medium into a transparent system with a limited field of view (c).

(Figure S5.a), programming successive phase ramps produces a shift of the focus on the camera, with no decrease in intensity. With the medium (Figure S5.b), shift of the focus is obtained by superimposing the phase ramps onto the optimized phase pattern. However, re-focusing persists only within a finite angular range with respect to normal incidence (Figure S5.c and Supplementary Movie M4). The finite-angle persistance of focusing is the memory effect (20).

Ratios between the intensity at focus $I^{(c)}(\boldsymbol{\theta})$ and the intensity measured at normal incidence $I^{(c)}(\mathbf{0})$, are represented in Figure S6. Without medium (Figure S6.a), the ratio is unity for all angles of illumina-

tion. With the medium (Figure S6.b), the ratio decreases with increasing illumination angle. Projections of the intensity ratios along both axis are shown in Figure S6.c. Values of the memory effect angular ranges $\Delta\theta_x = 1.08$ mrad and $\Delta\theta_y = 0.94$ mrad are estimated by fitting experimental results with a theoretical model provided in (36):

$$\frac{I(\theta)}{I(0)} = \left[\frac{\theta/\Delta\theta}{\sinh(\theta/\Delta\theta)} \right]^2 \quad (\text{S15})$$

The anisotropy observed between the two axis $\Delta\theta_x \neq \Delta\theta_y$ originates from the stress applied to the Parafilm when it is placed on the microscope slide.

6 Characterization of the optical memory effect of a thin scattering medium using spatially entangled photon pairs

This section provides additional information on the characterization of the optical memory effect with quantum illumination.

6.1 Decrease of the coincidence focus as a probe of the optical memory effect

When no medium is inserted in the experimental setup, the maximum of any conditional image $\Gamma(\theta_1|\theta)$, taken for an arbitrary angle θ , is reached for $\theta_1 = -\theta$ (Supplementary Movie M1). Moreover, the value of $\Gamma(\theta|-\theta)$ does not depend on the chosen angle θ [as it is shown in Figure S7.a in the particular cases of three different reference angles $\theta_D = (-0.67, 0.52)$ mrd, $\theta_E = (-0.67, 0.52)$ mrd and $\theta_F = (-0.67, 0.52)$ mrd]. When the medium is inserted and the optimized phase mask is programmed on the SLM, we observe that $\Gamma(-\theta|\theta)$ decreases when $|\theta|$ increases (Figure S7.b). Indeed, because of the memory effect, the two photons experience the medium as an almost transparent system if θ is small, while for larger angles their probability of being transmitted decreases because of the scattering (Figure 4.c). Since both photons are affected by this effect, the probability for them to be transmitted simultaneously at angles θ and $-\theta$ scales as the square of the probability for only one of them to be transmitted. The theoretical model describing the evolution of the probability ratio $\Gamma(-\theta|\theta)/\Gamma(0|0)$ is

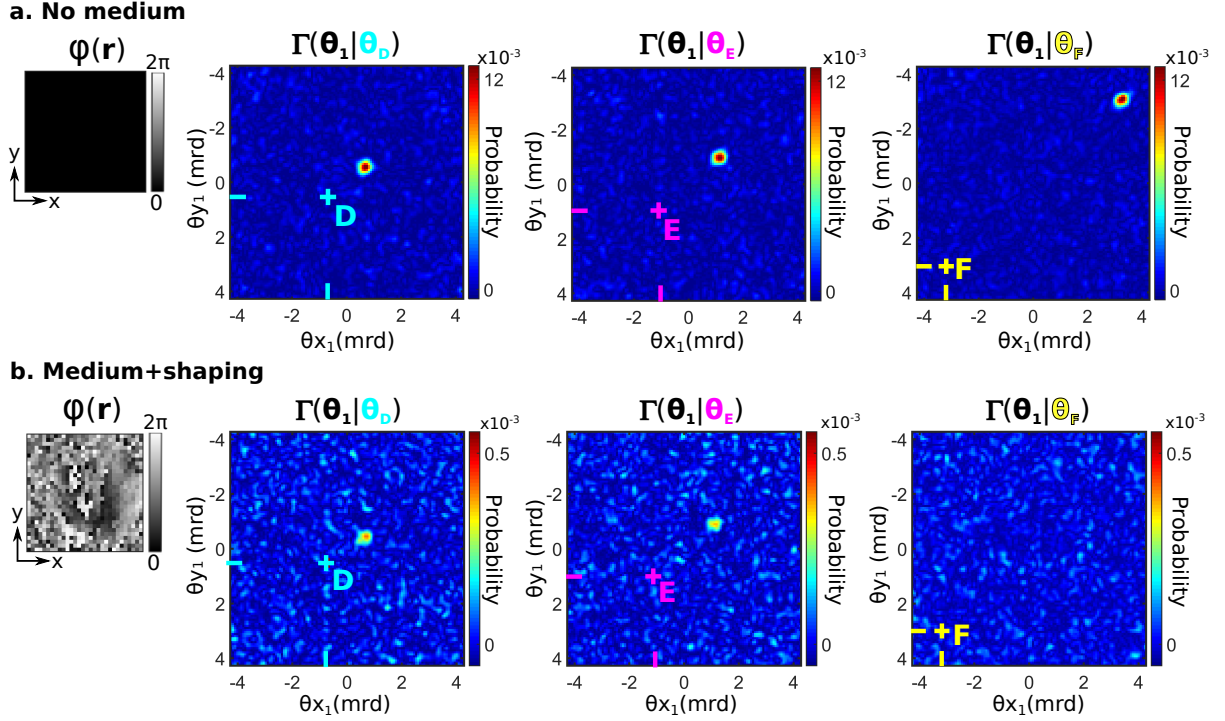


Figure S7: **Characterizing the optical memory effect of a thin scattering medium with quantum illumination.** (a) Conditional images $\Gamma(\theta_1|\theta)$ measured without the medium for three different values of the reference angle θ : $\theta_D = (-0.67, 0.52)$ mrd, $\theta_E = (-0.67, 0.52)$ mrd and $\theta_F = (-0.67, 0.52)$ mrd. After inserting the medium and programming the SLM, the same conditional images are measured (b) and show a decrease of $\Gamma(-\theta|\theta)$ with the increase of $|\theta|$, which is a signature of the optical memory effect of the scattering medium.

then directly established by squaring Equation S15:

$$\frac{\Gamma(-\theta|\theta)}{\Gamma(0|0)} = \left[\frac{\theta/\Delta\theta}{\sinh(\theta/\Delta\theta)} \right]^4 \quad (\text{S16})$$

The smaller angular width of the memory effect measured with quantum illumination (vs. classical light) is clearly visible on Figure 4.e.

6.2 Visualization of the memory effect along x axis

Figure S8 is the analogue of Figure 4 for the x axis. In this case, two lines of pixels are selected on either side of the center of the direct intensity image (Figure S8.a). Without the medium, projection of the joint probability distribution along these two lines $\Gamma(\theta_{x_1}, \theta_{x_2}|\theta_{y_1} = -0.07, \theta_{y_2} = 0.07)$ shows an

intense homogeneous anti-diagonal (Figure S8.b), which reflects the anti-correlated behavior of the pairs. After insertion of the medium and programming the SLM accordingly, the anti-diagonal is reconstructed only within a certain angular range $\Delta\theta_x$ (Figure S8.c). As shown in Figure S8.d, fitting the focusing ratio $\Gamma(\theta_x, \theta_{y_1} = 0 | -\theta_x, \theta_{y_2} = 0) / \Gamma(0|0)$ with the theoretical model provided in Equation S16 allows estimation of $\Delta\theta_x = 1.26 \pm 0.29$ (red curve). As a comparison, characterization of the memory effect performed with classical light is represented on the same graph (blue curve).

6.3 Complete mapping of the optical memory effect with quantum illumination

Probability ratios $\Gamma(-\theta|\theta) / \Gamma(0|0)$ measured for a large number of θ are shown in Figure S9. Without the medium, the ratio is unity for all angles (Figure S9.a). After inserting the medium and programming the optimized mask, we observe that the probability ratio $\Gamma(-\theta|\theta) / \Gamma(0|0)$ decreases in all directions with the increase of $|\theta|$ (Figure S9.b). Figure S9.c shows projections of $\Gamma(-\theta|\theta) / \Gamma(0|0)$ with (blue circle) and without (black circles) medium along both axis. Values of the memory effect angles measured with quantum light, $\Delta\theta_y = 1.01 \pm 0.1$ mrad and $\Delta\theta_x = 1.26 \pm 0.29$ are in good agreement with the values returned using classical light ($\Delta\theta_y = 0.93$ and $\Delta\theta_x = 1.08$ mrad).

7 Supplementary movies

Movie M1 Movie M1 shows a set of conditional images $\Gamma(\theta_1|\theta_2)$ taken at different reference positions θ_2 without the medium, with a flat phase on the SLM.

Movie M2 Movie M2 shows a set of conditional images $\Gamma(\theta_1|\theta_2)$ taken at different reference positions θ_2 without the medium, with a sine phase pattern programmed on the SLM.

Movie M3 Movie M3 shows a set of conditional images $\Gamma(\theta_1|\theta_2)$ taken at different reference positions θ_2 with the medium and the optimized phase pattern programmed on the SLM.

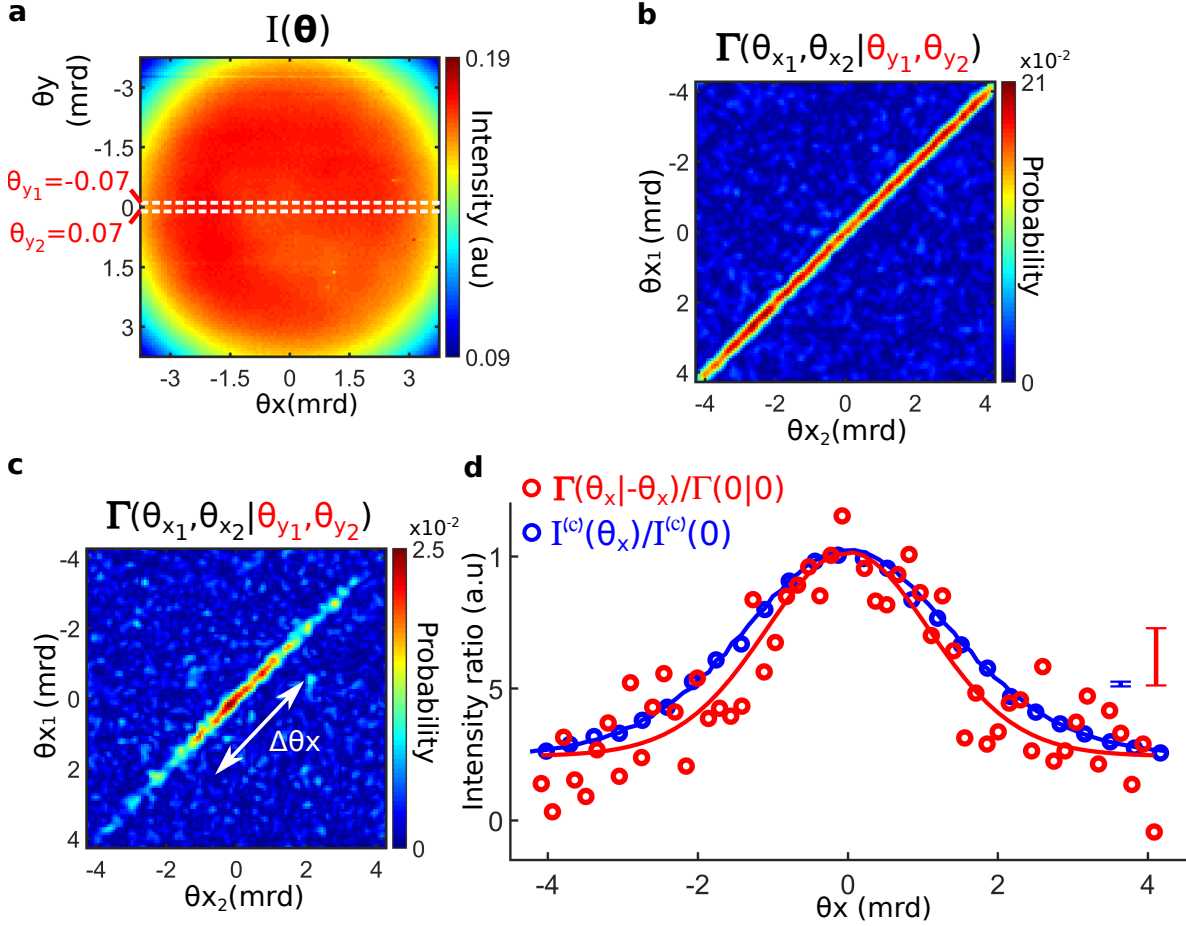


Figure S8: **Characterization of the optical memory effect along x axis using quantum illumination.** The joint probability distribution of photon pairs is projected onto two lines of pixel located at $\theta_{y1} = -0.07$ mrd and $\theta_{y2} = 0.07$ mrd (a). Without medium (b), $\Gamma(\theta_{x1}, \theta_{x2} | \theta_{y1} = -0.07, \theta_{y2} = 0.07)$ shows an intense anti-diagonal, that reflects the anti-correlation in the AS of photon-pairs. In the presence of the medium, the optimization technique reconstructs anti-correlations between pairs in a limited angular range $\Delta\theta_x$, which manifest itself as a reduction of the diagonal length (c). (d) Fitting the focusing ratio $\Gamma(\theta_x, \theta_{y1} = 0 | -\theta_x, \theta_{y2} = 0) / \Gamma(0|0)$ (red circles) with its corresponding theoretical model (red line) estimates $\Delta\theta_y = 1.26 \pm 0.29$ mrd. Classical measurement of the memory effect is represented on the same figure (blue circle) together with its corresponding theoretical model (blue line). Corresponding errors bars are shown on the graph.

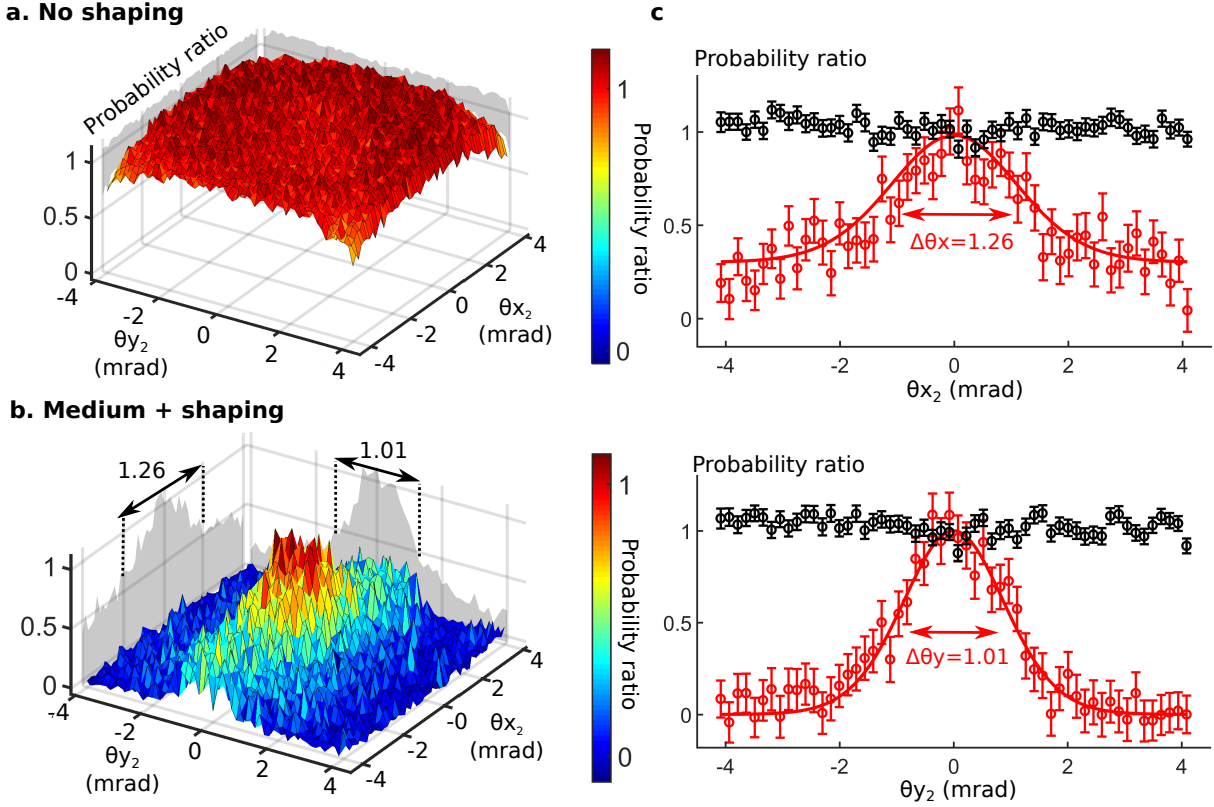


Figure S9: **Complete mapping of the optical memory effect with quantum illumination.** Map of probability ratios $\Gamma(-\theta|\theta)/\Gamma(\mathbf{0}|\mathbf{0})$ is reconstructed for a large number of θ when no medium (a) is inserted, and with a medium after optimization (b). Maps of the probability ratios are projected along both axes (c), with the medium (blue circle) and without the medium (black circles). Error bars are calculated by estimating the variance of the noise at each pixel using set of conditional images where the probability at this pixel is null.

Movie M4 Movie M4 shows shifting of the focus spot on the camera when the classical input beam is tilted by programming phase ramps on the SLM, without the medium.

Movie M5 Movie M5 shows shifting of the focus spot on the camera obtained after optimization through the thin scattering medium by superimposing phase ramps on the optimized phase mask.

Supplementary references

30. M. Reichert, H. Defienne, J. W. Fleischer, *arXiv:1802.00489* [physics, physics:quant-ph] (2018)

31. M. V. Fedorov, Y. M. Mikhailova, P. A. Volkov, *J. Phys. B: At. Mol. Opt. Phys.* 42, 175503 (2009).

32. P.-A. Moreau, J. Mougins-Sisini, F. Devaux, E. Lantz, *Phys. Rev. A* 86, 010101 (2012)

33. D. S. Tasca, et al., *Nature Communications* 3, 984 (2012)

34. J. C. Howell, R. S. Bennink, S. J. Bentley, R. W. Boyd, *Phys. Rev. Lett.* 92, 210403 (2004)

35. E. Small, O. Katz, Y. Silberberg, *Nature Photonics* 6, 549 (2012)

36. S. Feng, C. Kane, P. A. Lee, A. D. Stone, *Phys. Rev. Lett.* 61, 834 (1988)